

Article

Parametric Investigation of Parallel Deposition Passes on the Microstructure and Mechanical Properties of 7075 Aluminum Alloy Processed with Additive Friction Stir Deposition

L. P. Cahalan^{1,2}, M. B. Williams^{1,2} , L. N. Brewer³, M. M. McDonnell⁴ , M. R. Kelly⁴, A. D. Lalonde⁴,
P. G. Allison^{1,2}  and J. B. Jordon^{1,2,*}

- ¹ Point-of-Need Innovations (PONI) Center, Baylor University, Waco, TX 76704, USA; logancahalan@gmail.com (L.P.C.); brady_williams3@baylor.edu (M.B.W.); paul_allison@baylor.edu (P.G.A.)
² Department of Mechanical Engineering, Baylor University, Waco, TX 76704, USA
³ Department of Metallurgical Engineering, The University of Alabama, Tuscaloosa, AL 35487, USA; lnbrewer1@eng.ua.edu
⁴ U.S. Army DEVCOM Ground Vehicles System Center (GVSC), Warren, MI 48092, USA; martin.m.mcdonnell3.civ@army.mil (M.M.M.); matthew.r.kelly45.ctr@army.mil (M.R.K.); aaron.d.lalonde4.civ@army.mil (A.D.L.)
* Correspondence: brian_jordon@baylor.edu

Abstract: Large-scale metal additive manufacturing (AM) provides a unique solution to rapidly develop prototype components with net-shape or near-net shape geometries. Specifically, additive friction stir deposition (AFSD) is a solid-state method for large-scale metal AM that produces near-net shape depositions capable of high deposition rates. As AFSD is utilized for a broader range of applications, there is a need to understand deposition strategies for larger and more complex geometries. In particular, components with larger surface areas will require overlapping deposition passes within a single layer. In this study, the AFSD process was used to create depositions utilizing multiple passes with a varying deposition path overlap width. The effects of overlapping parallel pass depositions on the mechanical and microstructural properties of aluminum alloy 7075 were examined. The grain size and microstructural features of the deposited material were analyzed to evaluate material mixing and plastic flow in the observed overlap regions. Additionally, hardness and tensile experiments were conducted to observe the relationship between the overlap width and as-deposited material behavior. In this study, an ideal overlap width was found that produced acceptable as-deposited material properties.

Keywords: additive friction stir deposition; additive manufacturing; aluminum; dynamic recrystallization; parallel deposition pass



Citation: Cahalan, L.P.; Williams, M.B.; Brewer, L.N.; McDonnell, M.M.; Kelly, M.R.; Lalonde, A.D.; Allison, P.G.; Jordon, J.B. Parametric Investigation of Parallel Deposition Passes on the Microstructure and Mechanical Properties of 7075 Aluminum Alloy Processed with Additive Friction Stir Deposition. *Appl. Sci.* **2024**, *14*, 457. <https://doi.org/10.3390/app14010457>

Academic Editors: Vineet V. Joshi, David Field and Rajib Kalsar

Received: 14 November 2023
Revised: 21 December 2023
Accepted: 23 December 2023
Published: 4 January 2024



Copyright: © 2024 by the authors. Licensee MDPI, Basel, Switzerland. This article is an open access article distributed under the terms and conditions of the Creative Commons Attribution (CC BY) license (<https://creativecommons.org/licenses/by/4.0/>).

1. Introduction

Fusion-based additive manufacturing (AM) processes come with multiple complications when producing components from 7XXX-series aluminum alloys. The liquid-to-solid phase transitions sacrifice a large portion of the material's performance due to hot-cracking and the loss of intermetallic phases [1,2]. Friction-stir techniques provide a path forward by utilizing extreme plastic deformation at elevated temperatures without melting and resolidifying the material [3–5], thus promoting robust metallurgical bonding and improved mechanical properties. At the core, friction-stir approaches work by using a rotating tool to apply high shear forces to the material, thus generating friction, which leads to elevated temperatures and dynamic recrystallization within the microstructure [6–8].

Friction-stir techniques create different 'zones' within a material's microstructure. The material that is mixed by the tool is the dynamically recrystallized zone, or the 'nugget zone', which experiences the highest amount of plastic deformation and results in very small grain sizes. Just outside of the nugget zone is the thermo-mechanically-affected

zone (TMAZ), where the material undergoes plastic deformation and is exposed to large amounts of heat that is conducted through the material. The excess heat generated during this process affects the microstructure of the surrounding material, called the heat-affected zone (HAZ) [9–12]. In AFSD specifically, the nugget zone is denoted by the region of the base material directly deformed and mixed with the consumable feed rod, with the majority of the deposited material also characterized by dynamic recrystallization [13–16]. Some of the deposited material is pushed outward past the tool path profile or tool shoulder and is considered flash material. Flash material is primarily excess metal that is pushed aside as more material is deposited and the amount of flash generated is affected by the process parameters of the AFSD machine as well as the material properties [17]. Flash material is an important consideration, because it will have to be machined away later, which adds lead time to component production and reduces deposition efficiency.

The AFSD process has received increasing interest in recent years for its variety of applications and desirable as-deposited material properties. The AFSD approach is a solid-state process, where metallurgical bonding between each layer is achieved while avoiding the solid-to-liquid phase change [18]. The solid-state nature of friction-stir processes enables the processing of materials that are sensitive to thermomechanical effects, such as precipitate-strengthening in 7XXX-series aluminum alloys [19–21]. For 7XXX-series aluminums, the typical operating temperature holds below 85% of the material's solidus temperature during the AFSD process. The AFSD process is a low-power, open-atmosphere process with high deposition rates for aluminum alloys, which naturally lends itself to point-of-need component repair and near-net shape additive manufacturing in austere environments [22–25].

There have been several studies that investigated the as-deposited material properties of large-scale AFSD builds, and the associated effects of intersecting deposition regions, where material is deposited through or alongside previously deposited material. A study performed by Mason et al. (2021) focused on the effect of the mechanical and microstructural properties of intersecting perpendicular deposition paths, creating a region where previously deposited AA7050 material would undergo dynamic recrystallization a second time, and discovered that this 'crossover region' had comparable material properties to the 'transient region', which was not overlapped [19]. An experiment performed by Robinson et al. (2022) explored a large-scale AFSD build with parallel, tangent deposition paths with no overlapping material and reported near-wrought material strength in an as-deposited magnesium alloy build, showing that these friction-stir processes are scalable to larger volumes of material [26]. Studies by Al-Fadhalah et al. (2014) and Ma et al. (2006) have investigated the effect of multi-pass friction stir welding (FSW) on microstructure and mechanical properties and have concluded that the excess heat generated during a prolonged friction-stir process has a negative impact on as-processed material strength [27,28]. Al-Fadhalah and Ma also reported that these materials, once heat-treated, performed similar to the as-received base aluminum material.

In another study, Phillips et al. (2021) explored the specific impact of a partially overlapping parallel deposition path to create an overlap region width of 6.35 mm. Phillips investigated the tensile properties of this region, while also examining the microstructural impact that an overlap region would have on deposited AA6061 material [29]. Phillips's investigation of a single overlap width reported a slight improvement in as-deposited tensile strength in the overlap region compared to a single-row deposition of the same material, overcoming the negative impact on material strength reported in multi-pass FSW studies. Phillips also observed the formation of oxides at the interfaces between the deposition paths and the substrate.

This study investigates the relationship between overlapping deposition tracks of AFSD and the resulting as-deposited mechanical properties and microstructure of aluminum alloy 7075 (AA7075). In order to carry out this investigation, microstructural analysis was performed using optical light microscopy on chemically etched cross-sections taken from the depositions with vary overlaps widths. Mechanical testing was then con-

ducted on specimens taken from the overlap samples to evaluate the hardness, quasi-static tensile strength, and ductility of the as-deposited material. Finally, post-mortem fractography analysis using scanning electron microscopy (SEM) was performed to qualitatively evaluate the fracture mechanisms of varying overlap deposition paths of AFSD.

2. Materials and Methods

AA7075 is a commonly used material in the aerospace, automotive, and defense industries due to its high strength-to-weight ratio and corrosion-resistant properties [30,31]. For this study, extruded AA7075-T6 rods were used as the feedstock material, and machined AA7075-T6 plates were used for the substrate material. AA7075 is an Al–Zn–Mg–Cu precipitate-strengthened alloy that derives its strength primarily from the formation of η' phases [32,33]. The T6 temper generates relatively high strength due to the ideal generation of the Mg_2Zn and Al_2CuMg strengthening precipitates [34,35]. This alloy was chosen for the present study for its industry relevance and to allow for direct comparison to prior friction-stir processing studies [36–38].

Figure 1a shows a schematic of an AFSD build with geometry similar to depositions used in this experiment. A non-consumable hollow cylinder tool is rotated at high RPM (ω) in tandem with a linear actuator applying a downward force, relative to the build direction, to the end of the consumable feed rod at the desired feed rate (f). As the tool traverses at a constant speed (v) over the substrate material, the feed rod material is deposited and mixed with the substrate. As shown in Figure 1b, during the second traverse in the longitudinal direction, a region of the recently deposited material is processed a second time in the overlap region.

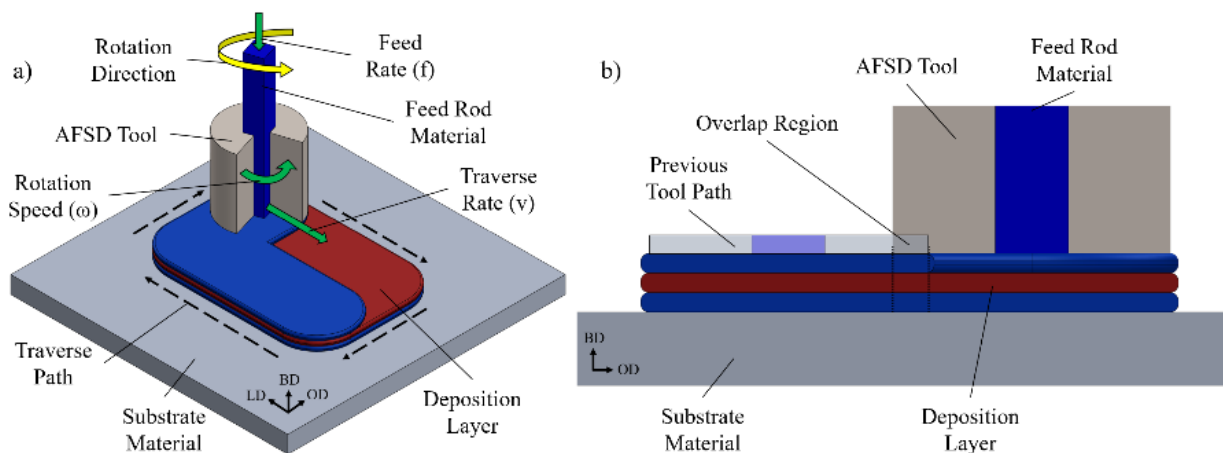


Figure 1. (a) Representative schematic of an in-progress parallel pass AFSD. (b) Section view with overlapping tool path schematic. Red and blue coloration is used to visually distinguish deposition layers.

At the start of each layer, the tool dwells in place, generating the frictional heat and high shear forces required to achieve plastic flow. The tool dwells in the same position at each layer, located in the nearest corner of the build in Figure 1a, until the feedback force is measured by the linear actuator stabilizes, signifying the material has achieved plastic flow. Once the material has reached the necessary temperature, between 350° and 400° Celsius [17], and the feed rod is able to plastically deform with relatively low force, and the tool begins traversing in the longitudinal direction (LD) and deposits the initial pass of material. The tool then moves orthogonally in the overlap direction (OD) until the center of the tool reaches the predetermined distance to create an overlap region of the desired size. The tool then travels parallel to the initial pass, but in the opposite direction, to deposit the return pass. During the return pass, a portion of the initial pass deposition is subjected to extreme plastic deformation a second time, mixing with the new material being deposited. The tool face then returns to the dwell zone before moving in the

vertical build direction (BD) and begins the next layer in the same movement pattern. In this present study, the tool path is always followed in a clockwise pattern.

During the AFSD build process, the rotation of the tool face causes non-uniform material flow. The advancing side (AS) is the side where the tangent line of the tool face's rotation is aligned in the same direction as the traversing direction of the tool's movement. The retreating side (RS) is the opposite side of the tool face, where the tangent line is parallel to the traverse direction, but opposite in magnitude. The tool face rotates in a counterclockwise direction throughout the entire deposition. This means that the center of the build, where material is overlapped, is always on the advancing side of the tool face in this present study.

Figure 2a shows a model of the 38.1 mm diameter tool used in this study. This tool, made of H13 tool steel, has multiple 'teardrop' protrusions that generate additional shear force and friction in the substrate material. These protrusions allow the material to quickly approach the temperatures necessary for plastic flow and improves mixing within the material. Figure 2b shows a drawing of the tool face with critical dimensions. The tool face protrusions extend 2.08 mm downward from the face of the tool, which allows for improved mixing between deposition layers. This tool design has been used in similar AFSD overlap studies [29,39].

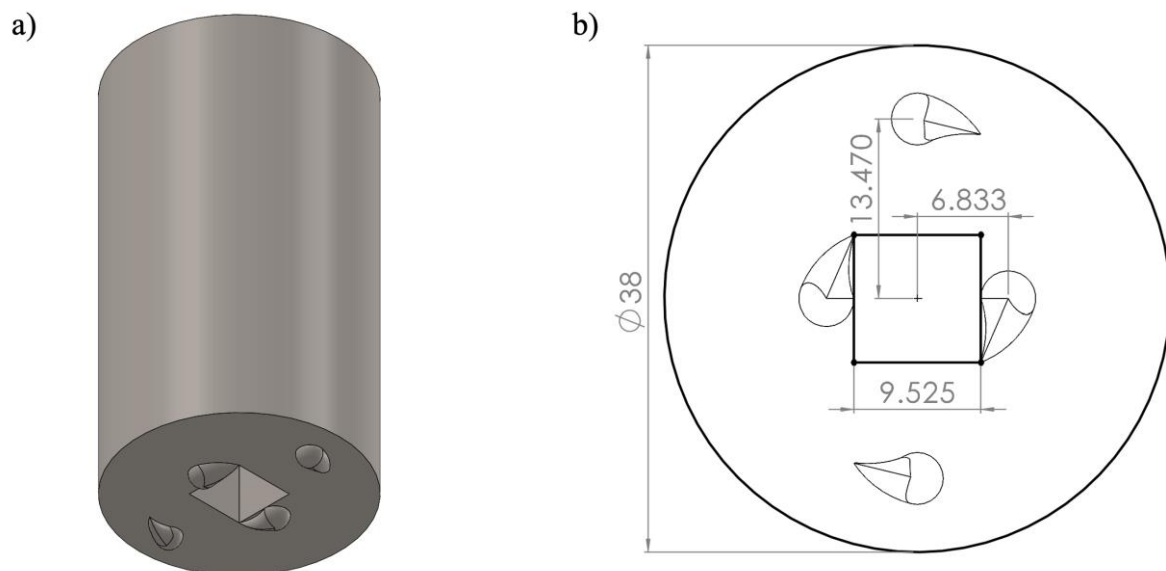


Figure 2. (a) Representative model of the AFSD tool. (b) Dimensioned schematic of the AFSD tool face in mm.

Table 1 details the nominal size and features of the overlap region for each build, which determines the amount of mixed material and overall size of the build used in this study. The 'center-to-center distance' refers to the distance between the center of the tool face during the initial pass and during the return pass. The tool face has a diameter of 38.1 mm, so a center-to-center distance of 38.1 mm would have no material overlapping and there would be no gap between the tool path of the initial deposition pass and the returning pass (Build C). The 'overlap region width' refers to the distance between the edges of the paths of the initial and returning passes, which is equal to the center-to-center distance subtracted from the tool face diameter. A negative overlap width, such as Build A and Build B, would instead have a gap between the deposition passes. The operating parameters used in this study resulted in this gap being partially filled with flash material. This value was increased from an initial gap of 6.4 mm (−6.4 mm overlap), which is equal to one-third of the radius of the tool face, to an overlap of 19.1 mm, equal to the radius of the tool face, at an increment of 3.2 mm. These parameters chosen in this study were based on the geometry of the tool face, specifically the tool radius, as well as the location of the

‘teardrop’ protrusions shown in Figure 2b. The ‘volume per build’ details the total volume of completed deposition based on the geometry of the tool path, diameter of the tool face, and the build height of four 1 mm layers and excludes the flash material on the outside of the build, which would be machined away in practical applications. The ‘single-layer deposition time’ refers to the number of seconds necessary for the tool to traverse the pre-programmed path as it deposits a single rectangular layer.

Table 1. Overlap build parameters.

Build	Center-to-Center Distance (mm)	Overlap Region Width (mm)	Volume Per Build (cm ³)	Single-Layer Deposition Time (s)
A	44.5	−6.4	39.8	102.0
B	41.3	−3.2	38.4	99.0
C	38.1	0.0	36.7	96.0
D	34.9	3.2	35.2	93.0
E	31.8	6.4	33.8	90.0
F	28.6	9.5	32.1	87.0
G	25.4	12.7	30.6	84.0
H	22.2	15.9	29.2	81.0
I	19.1	19.1	27.5	78.0

Table 2 details the process parameters of the AFSD machine that remained consistent between each build. These parameters include the tool rotation speed, material feed rate, and tool traverse rate. The build rate is calculated based on the volume of material deposited at these settings. Deposition pitch provides a way to quantify mechanical mixing and is derived from the traverse rate and tool rotation speed. Average heat input, H , is calculated as:

$$H = \frac{2\pi \times \tau \times \omega}{60 \times v} \quad (1)$$

where τ is the average spindle torque recorded by the AFSD machine, ω is the tool rotation speed, and v is the traverse rate of the AFSD tool. Each build was deposited on a square build plate with side length 152.4 mm and a thickness 9.5 mm machined from an AA7075-T6 plate. The deposition is made from AA7075 feed rods that are 304.8 mm in length and have a square cross-section with a side length of 9.5 mm and a graphite coating as prescribed by the MELD B8 operating manual to eliminate jamming of the feedstock material during depositions. The build pattern is a rectangle with the traversed distance in the overlap direction varying between 44.5 mm and 19.1 mm, as shown in Table 1, with a consistent distance in the longitudinal direction of 63.5 mm. These dimensions are based on the distance traveled by the center of the tool face during the deposition.

Table 2. AFSD machine operating parameters.

Parameter	Variable	Units	Value
Tool speed	ω	RPM	275.0
Feed rate	f	mm/min	69.9
Traverse rate	v	mm/min	127.0
Build rate	R	kg/hr	0.8
Deposition pitch	P	rev/mm	2.2
Average heat input	H	MJ	1.1

Figure 3 shows top-down images of the nine depositions made in this study. Figure 3a–i correspond to the parameters detailed in Table 1. All nine builds were deposited using the parameters detailed in Table 2. With these builds, it is easy to see the drastic difference in build volume between a build with no overlap, such as Builds Figure 3a,b, compared to a build with a higher amount of overlapping material, such as Builds Figure 3h,i. Only one trial for each overlap distance was deposited for the present study.

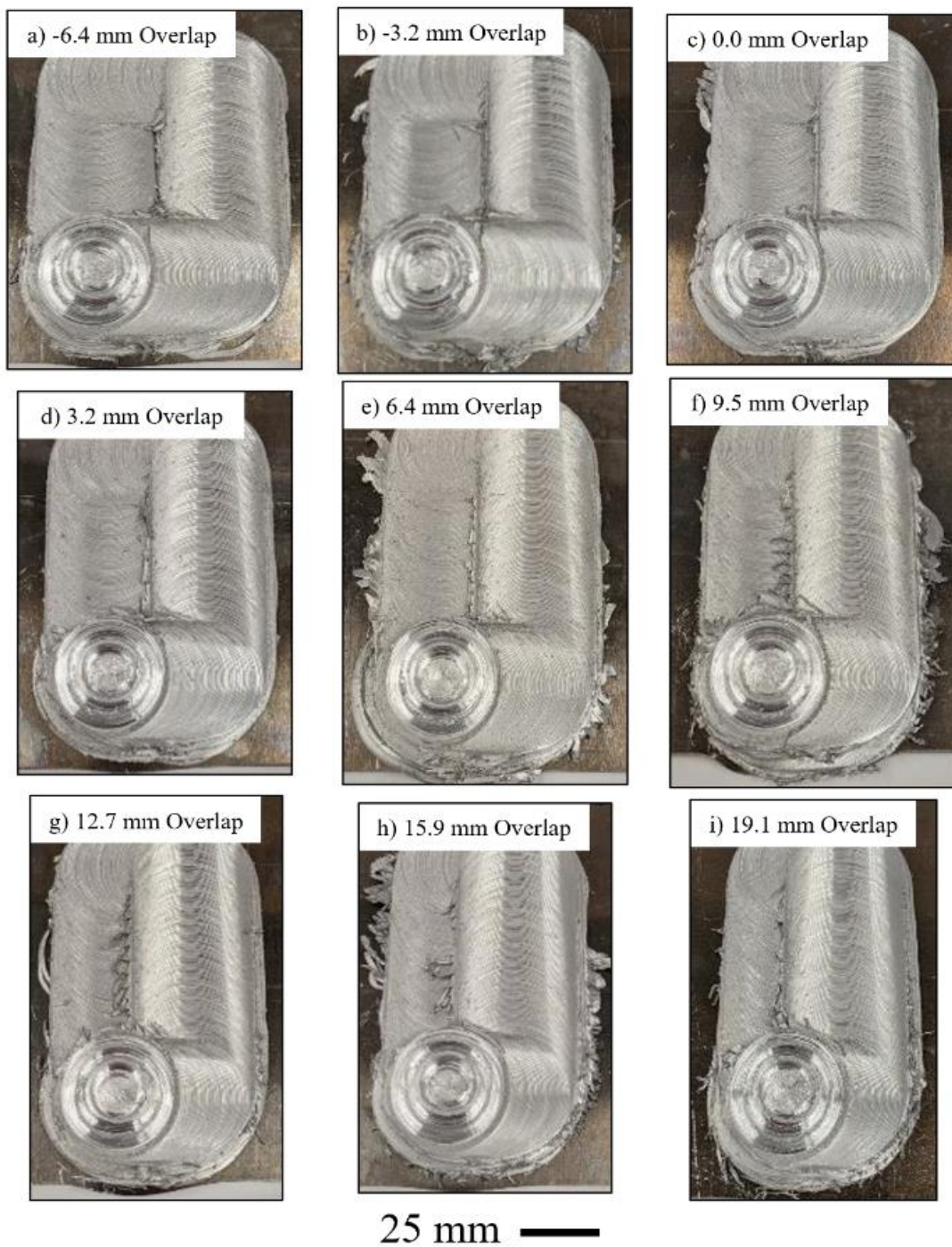


Figure 3. Completed AFSD builds with variable overlap widths.

If a component was to be made with a much larger surface area than the depositions from this study, there would be a large difference in the required amount of consumed material between builds using different overlap parameters, assuming all other operating parameters are held constant. A large build using a 6.4 mm overlap (Figure 3e) would take much less material and time, and therefore require lower overall costs, than a build with a 19.1 mm overlap (Figure 3i). A build using a gap between passes instead of an overlap, such as Figure 3a, with a -6.4 mm overlap, would deposit material the fastest and use the least amount of material, but the mixing region between the initial and returning pass would only be connected by the flash material. A greater amount of overlap will have a much higher amount of mechanical mixing and create a more homogenous deposition

throughout the multiple deposition tracks at the expense of more material and a longer build time.

From the builds shown in Figure 3, tensile specimens and cross-section samples were collected for quasi-static tensile testing, hardness testing, and grain size analysis. Figure 4a shows the schematic of a completed build with the original locations of the tensile specimens and cross-section samples. The build shown was deposited with a 3.2 mm overlap, which corresponds to Build D from Table 1 and Figure 3d. The failure location of each specimen was designed to be within the overlap region of the deposition. Figure 4b details the dimensions of the tensile specimens used in the present study in accordance with the modified ASTM E606/E606M-12 standard [40]. Due to the geometry of the tensile specimens and the final depositions, quasi-static results could not be collected for every build.

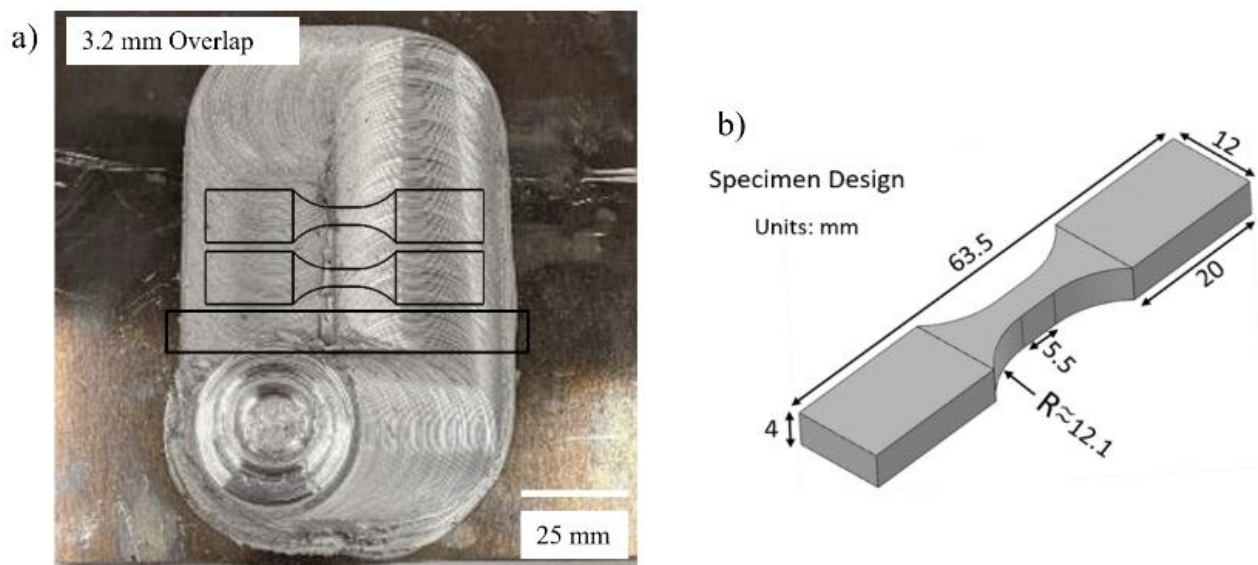


Figure 4. (a) Representative AFSD overlap build with a tensile specimen layout schematic. (b) Dimensioned model of the tensile specimen.

Specimens and cross-sections were machined from the respective depositions using a Mitsubishi MV1200 wire electron discharge machine. The specimens were tested using a 25 kN Landmark 370 MTS servohydraulic load frame and were run in displacement control with a 5 mm gauge extensometer at a nominal strain rate of 0.001 s^{-1} in ambient laboratory conditions. Post-mortem specimen analysis was performed via scanning electron microscopy (SEM) using a Versa 3D focused ion beam scanning electron microscope for -3.2 mm overlap specimens and a TM3030 Plus tabletop scanning electron microscope for all other specimens.

All hardness measurements were taken using an EMCOTest DuraScan 50 microhardness tester, in accordance with ASTM E384-22 [41], with a load of 2 newtons and a 10 s load period (HV 0.2). Hardness data was collected across the entirety of each cross-section in a grid pattern with 1 mm spacing between data points. Grain size analysis was performed using the line-intercept method in compliance with the ASTM E112-13 standard [42]. Grain size and microstructure analysis was performed using a Keyence VHX-7100 digital microscope for all cross-section samples.

3. Results

Figure 5 shows representative cross-sections of three different builds with schematics of the tool face position superimposed on the deposition cross-section to illustrate the location of the tooling relative to the final depositions. These cross-sections are scaled to the same proportions, and it can be observed that as the overlap value increases, the width of

the build decreases, similar to the observations made from the builds in Figure 3. Figure 5a shows the tool face schematic for a build with a 6.4 mm gap, corresponding to Build A from Table 1 and Figure 3a. This build can be clearly seen as two distinct depositions with their own TMAZ and HAZ that appear to be the most intense beneath the ‘nugget zones’ of the deposition paths. The boundary between the TMAZ and HAZ can be observed in the microscopy image as there is a clear distinction between the refined grains undergoing recrystallization within the TMAZ and the much larger grains of the base material within the HAZ. The material between the depositions is flash material that makes contact between the deposition paths but does not experience any mixing. Figure 5b shows the schematic for a build with a 6.4 mm overlap, corresponding to Build E from Table 1 and Figure 3e. In Figure 5b, there is not a clear boundary in the deposited material between the two passes, but there is instead a central interface region where there is a large amount of mixing between the two passes. Figure 5c shows the schematic for a build with a 19.1 mm overlap, corresponding to Build I from Table 1 and Figure 3i. In this build, the mixing zone of the overlapped region follows the flow pattern of the retuning deposition pass, giving a more distinct interface boundary of the mechanically affected zones for each deposition pass.

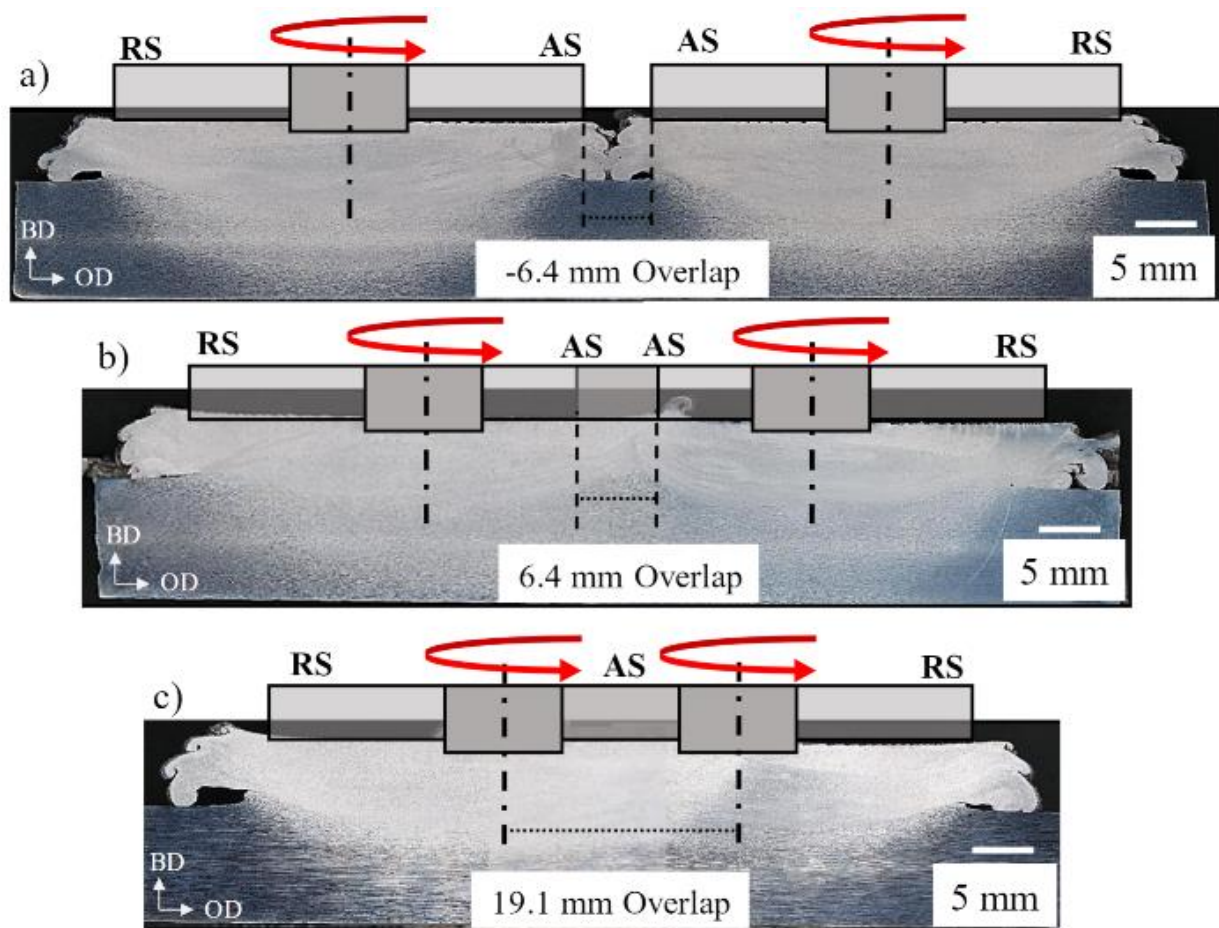


Figure 5. (a–c) Representative etched cross-sections with tool profile schematics of the AFSD overlap builds.

Figure 6 shows the overlap interface regions for each build, where the two regions of deposited material are mixed and bonded together. Figure 6a–i correspond to the build parameters detailed in Table 1. Using optical microscopy on the etched cross-sections of each build, the material flow at the overlap boundary interface can be visualized clearly. In Figure 6a (−6.4 mm overlap), 6b (−3.2 mm overlap), and 6c (0.0 mm overlap), distinct swirling patterns are present in the flash material as the depositions are pressed together.

There was minimal mixing in these builds, so a clear boundary between deposition passes can be observed. In Figure 6d–i, the interface material was mixed during the deposition of the return pass, so the flash material, as well as a portion of the initial deposition layer, was mixed with the new material. This makes a defined boundary between the deposition passes difficult to identify and causes the swirling pattern to become blended and deformed within the cross-section. The cross-sections show an increasing level of mixing between deposition layers and passes because while the swirling pattern is still visually present in each cross-section, the boundary becomes less distinct as the overlap distance increases. A build with a large overlap region will have to force more pre-existing material outward as new material is deposited. Additionally, the interface boundary at the edge of the initial deposition pass is consumed as part of the TMAZ of the return pass. This means the interface is subjected to high amounts of shear force and plastic deformation as new material is deposited, eliminating any distinct interface boundary and creating a more homogeneous material.

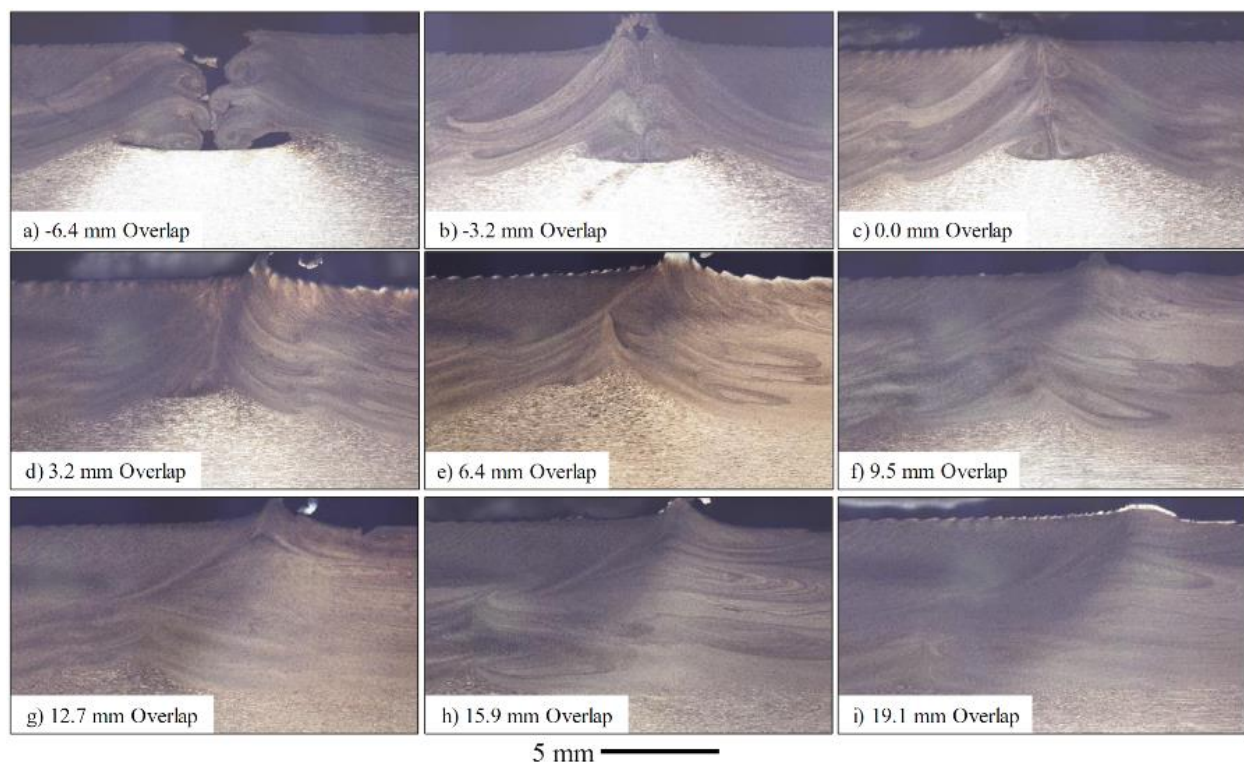


Figure 6. (a–i) Etched cross-sections of the AFSD overlap interface regions.

In addition to mixing between deposition passes, substrate deformation can be seen in many of the cross-sections shown in Figure 6. As the substrate material near the surface interacts with the tool face, a portion undergoes dynamic recrystallization, creating a gradient region within the TMAZ. The geometry of this gradient is due to the teardrop protrusions on the tool face and can be visualized in Figure 5, where the nugget zone extends deeper into the substrate near the center of the tool path. The substrate material that does not dynamically recrystallize is still subjected to high levels of plastic deformation as part of the TMAZ, and partially mixes with the deposition. This wave-like deformation is best observed in Figure 6c, where substrate material appears to be pulled and lifted above some of the deposited material near the interface.

Figure 7 provides a higher magnification image of the overlap interface region for a build with a -3.2 mm overlap width. This corresponds to the build shown in Figures 3b and 6b and Build B from Table 1. Figure 7a shows the same region as Figure 6b but is focused only on the interface. Figure 7b–d were captured using optical microscopy

on the top, center, and bottom of the deposition interface, respectively. These images were taken at a high enough magnification to visualize individual grains ranging from the relatively elongated grains of the substrate to the sub-micron grains located at the very edges of the deposited material.

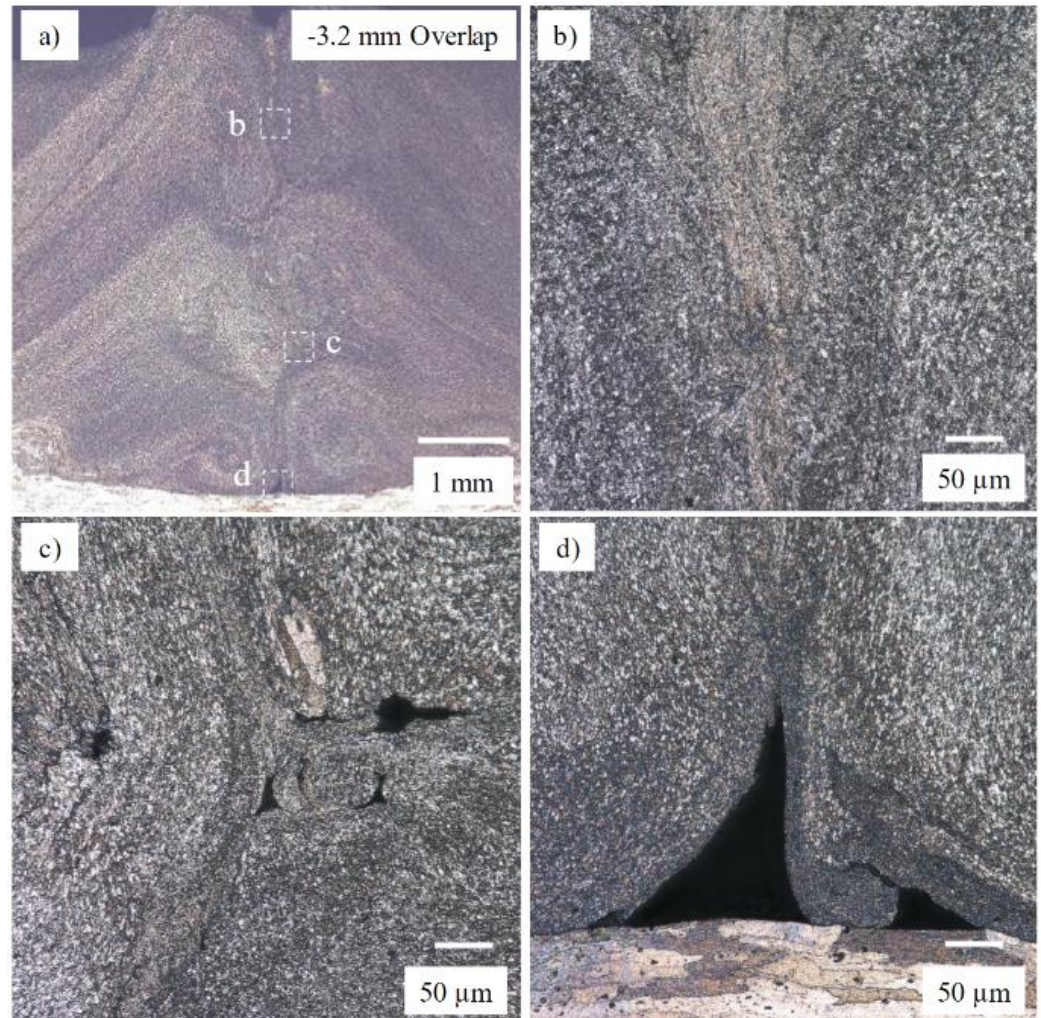


Figure 7. (a) Etched cross-section of the -3.2 mm AFSD overlap interface region. (b–d) High magnification of the top, middle, and bottom of the interface boundary.

This interface region exists in a gap between the initial and return deposition passes, and therefore does not experience the high levels of plastic deformation that the rest of the deposition is subjected to. Material forced into this region can only be exposed to other material that has been pushed out from the deposition, meaning that it is only subjected to relatively low compressive forces instead of the extreme shear forces caused by the tool face. This allows the flash material to maintain the swirling effect observed in the cross-sections with an overlap width of 0.0 mm or less. The swirling pattern observed in this present study has also been reported by Phillips et al. (2021) [29], where a ‘pluming’ effect was seen at the interface of the tested overlap region of 6061 aluminum alloy. Flash material that is pushed aside during the deposition tends to curl downward towards the substrate as it extends past the deposition, as observed on the outer edges of the cross-sections shown in Figure 5. When depositing with an overlap, the flow of the material is physically constrained, forcing the flash into a tighter curl at the interface, emphasized by the visual effect of the plumes observed in these experiments.

A ‘seam’ can be observed throughout each Image of Figure 7 that denotes where the two deposition passes meet and are forced against each other as the material flows

outward from the tool path. In Figure 7b–d, the interface boundary contains very small grains compared to the rest of the deposited material. Also present at the interface are several relatively large voids, seen clearly in Figure 7c,d. These voids show that the flash material does not experience enough forces to properly mix and bond with the other side of the interface. The region shown in Figure 7b does not contain these voids because the material here has experienced higher compressive forces as the plumes flow into each other compared to the region in Figure 7c, where the plumes flow around each other.

Figure 8 captures a similar region as Figure 7, but for the cross-section of a 0.0 mm overlap build, corresponding to Figures 3c and 6c and Build C from Table 1. Figure 8b–d are taken from the top, middle, and bottom of the interface, respectively. Much like Figure 7, the pluming effect is clearly visible in this cross-section, as well as the ‘seam’ along the interface boundary where the flash material is compressed together, although this sample shows a much more vertical interface boundary due to the material having less space to flow with the smaller gap size between deposition paths.

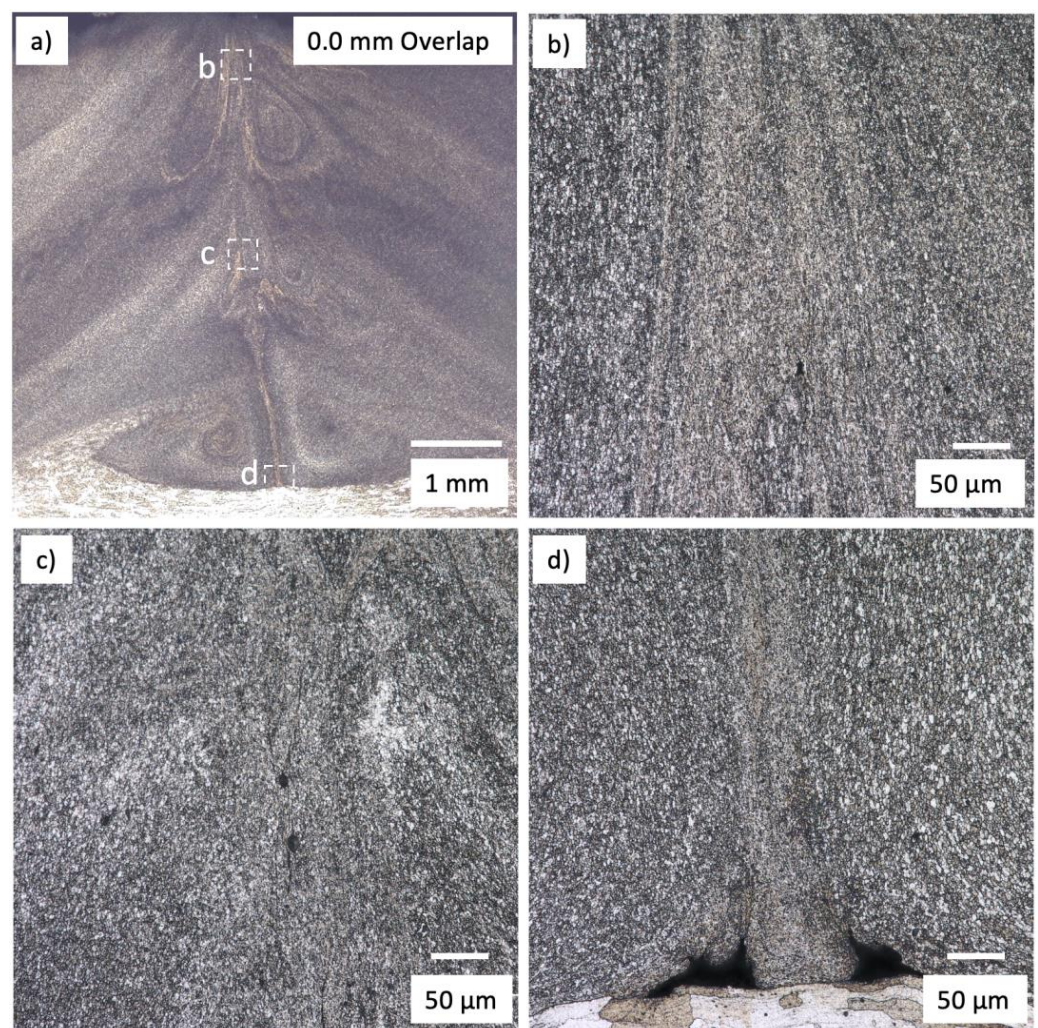


Figure 8. (a) Etched cross-section of the 0.0 mm AFSD overlap interface region. (b–d) High magnification of the top, middle, and bottom of the interface boundary.

Figures 7b and 8b have a similar appearance, where the two deposition zones are pushed together to create a boundary zone where, although mixing does not occur, there appears to be a somewhat effective amount of compressive bonding. This interface also shows relatively smaller grains at the edges of the deposited material, as well as relatively small voids compared to those observed in Figure 7c. The voids in Figure 8b,c are indicated within the dashed circles. Figure 8c appears to be similar to Figure 8b, but a few small

voids located at or near the interface boundary can be observed. While there are still multiple voids visible in this sample, they are within the range of five to ten microns in diameter, which is much smaller than those observed in Figure 7c, which ranged from ten microns to over fifty microns in diameter. A previous study by Jordon et al. [43] observed the porosity of an AA7075-T651 plate and reported an initial void radius of 11.2 microns (22.4 microns in diameter) prior to crack growth. The interface boundary is still clearly defined, with multiple voids and several crack-like features visible in the microstructure, but is much more uniform than the interface shown in Figure 7. This trend continues where the deposited material meets the substrate in Figure 8d, as two relatively large voids are present, and bonding with the substrate material does not occur at the overlap interface. It can be observed that while the material is forced together and potentially bonded, there is not enough mechanical mixing between the initial and return deposition passes for these cross-sections with a non-positive overlap width to form a homogenous material.

In addition to qualitative evaluation of the effect of a varying overlap region width, quantitative mechanical testing was performed on each build. Figure 9 shows the heat maps of the Vickers hardness of the cross-sections with varying overlap distances. There is a clear trend showing that the HAZ within the substrate is softer than the deposited material, forming a gradient between the top of the deposition and the substrate material. Many cross-sections also show that the initial pass (shown on the right side of each figure) has a lower hardness than the returning pass (shown on the left side of each figure). The TMAZ of the return pass mixes with a portion of the initial deposit, causing a uniform TMAZ for the return pass, while subjecting the initial deposition pass to additional heat. This new HAZ not only negatively impacts the previously deposited material, but also subjects the substrate and previous layers to large amounts of heat over a much longer period of time when compared to a single-pass deposition.

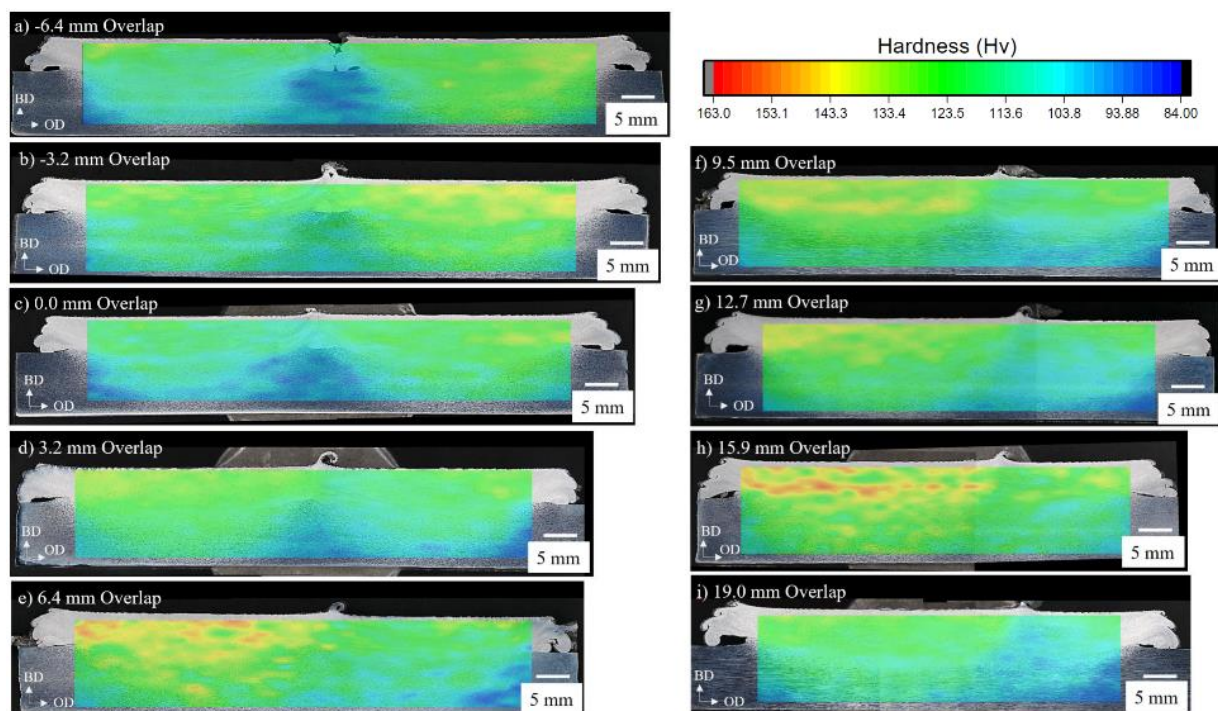


Figure 9. (a–i) Cross-sectional images of AFSD builds with varying overlapping parallel deposition passes. Additionally, the experimental hardness maps corresponding to each AFSD build are shown overlaid for each cross-sectional image.

Table 3 shows the average hardness for the deposited material in each build compared to the width of the overlap region. While data was collected for the entire sample to compare the deposited, substrate, and transition zone material, only data from the deposition

material is shown in Table 3. No apparent correlation between the hardness of the deposited material and the overlap region width was observed. This is expected, as all process parameters aside from the overlap region width were held constant between depositions. Some of the builds, such as the 6.4 mm overlap and 15.9 mm overlap builds, shown in Figures 9e and 9h, respectively, were recorded to be relatively harder than the other builds, but these values fall within the expected variation.

Table 3. Average Vickers hardness of the deposited AA 7075.

Overlap Region Width (mm)	Average Deposition Hardness (Hv)
−6.4	123.0
−3.2	128.9
0.0	127.9
3.2	126.0
6.4	132.5
9.5	128.6
12.7	127.3
15.9	135.0
19.1	121.1

Figure 10 shows the locations used for grain size analysis. For each cross-section, multiple locations were selected from the deposited material near the interface boundary. As shown in Figures 7 and 8, grain size can vary dramatically in certain regions of the build, with relatively large grains still present in the substrate, and very refined grains observed at the edges of the flash material. For this analysis, grain size was investigated in the dynamically recrystallized deposition material near the overlap interface but excluded the flash material which would be machined away in practical applications.

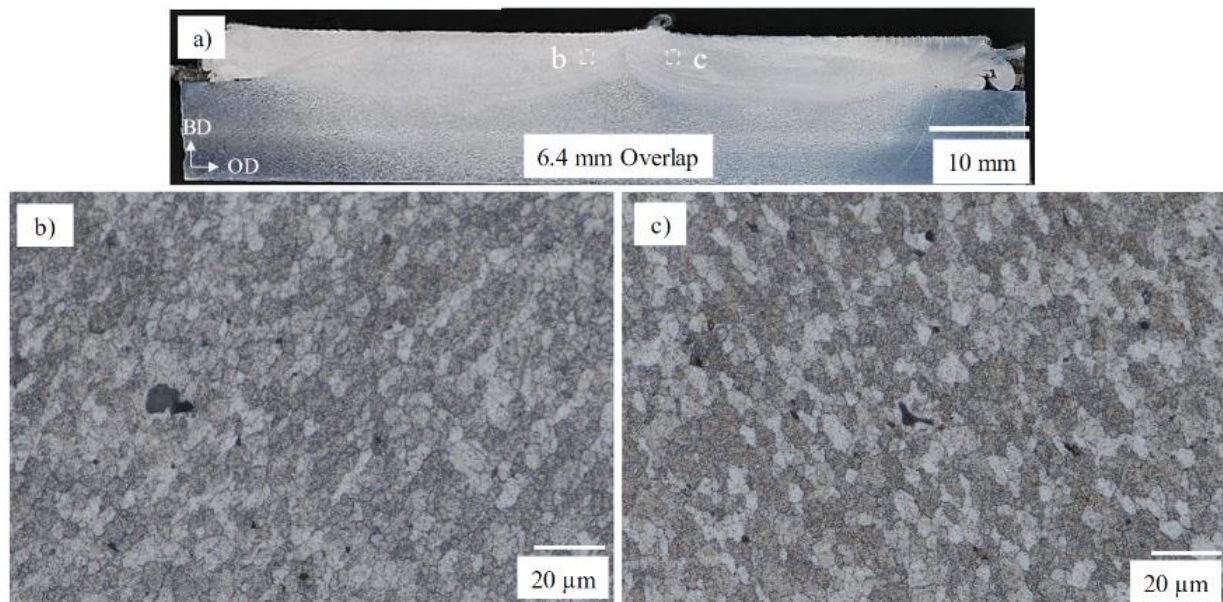


Figure 10. (a) Cross-section of the 6.4mm AFSD overlap sample with selected regions for grain size analysis. (b,c) High magnification images used for grain size analysis.

Figure 11 displays the relationship between the grain size and the deposition overlap distance, measured in mm, with the recorded scatter included for each cross-section. A negative overlap distance corresponds to a gap of the same magnitude. Although some of the tested regions have a relatively wide range of scatter, with the largest range being slightly larger than 1 μm, the average grain size remains consistently between 4 and 4.5 μm across all cross-sections. Similar to the collected hardness data, there is no observed trend

relating grain size to overlap region width. This is expected, as all process parameters aside from the overlap region width were held constant between depositions. The observed range of grain sizes is also within the expected range for a 7XXX-series aluminum alloy processed with AFSD [39].

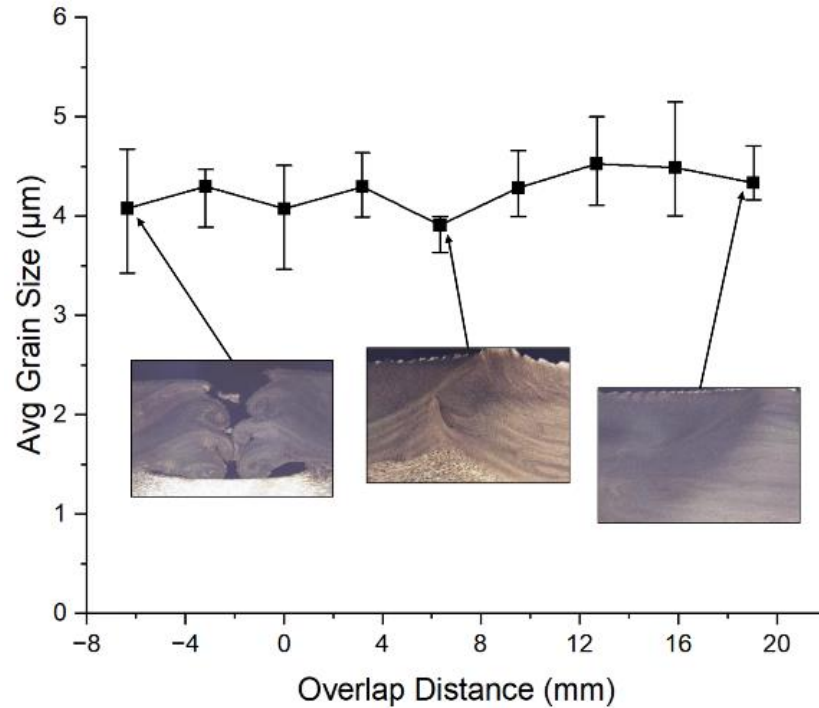


Figure 11. Grain size as a function of overlap distance in the AFSD builds.

Table 4 details the experimental results of tensile testing including the yield strength and ultimate tensile strength, measured in megapascals, and the elongation to failure, measured in percentage, for each tested AFSD overlap specimen. Additionally, Figure 12 shows the engineering stress-strain results for each tested AFSD overlap specimen. As expected, since the as-deposited materials were no longer in the T6 condition, the feedstock material exhibited higher yield and ultimate strength compared than the as-deposited material specimens. As the AFSD build is deposited, the material experiences relatively high temperatures for an extended period of time. This causes the feedstock material to undergo precipitate coarsening, which effectively removes the benefits of the T6 heat treatment from the material during the deposition process [39]. Because the completed builds were not heat-treated before the mechanical testing was conducted, this difference in tensile strength is expected. Due to geometric constraints, specimens could not be collected for every deposition, and two tensile specimens were collected from each tested build.

Table 4. Numerical data for quasi-static results.

Specimen	YS (Mpa)	UTS (Mpa)	EF (%)
−3.2 mm overlap (A)	247	405	9.8
−3.2 mm overlap (B)	N/A	N/A	N/A
0.0 mm overlap (A)	229	258	1.5
0.0 mm overlap (B)	249	346	5.0
3.2 mm overlap (A)	266	360	3.8
3.2 mm overlap (B)	264	387	6.6
9.5 mm overlap (A)	299	434	7.2
9.5 mm overlap (B)	290	426	7.8
Feedstock	525	583	19.0

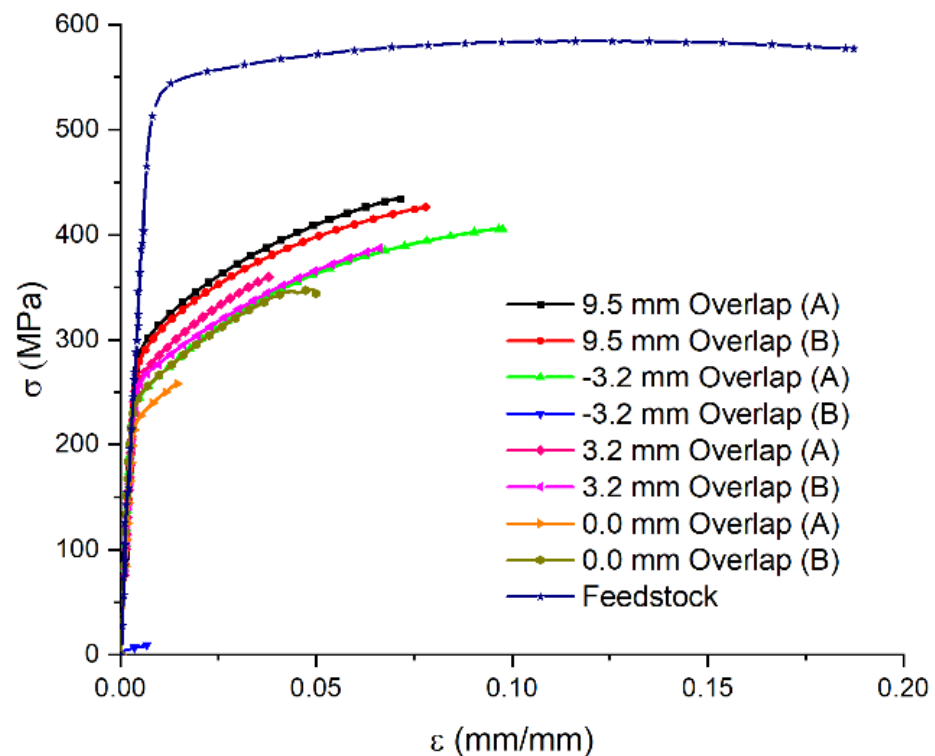


Figure 12. Quasi-static data for AFSD overlap specimens compared to feedstock AA7075.

The yield strength, ultimate strength, and ductility all show favorable improvement as the overlap width increases across almost every specimen tested. The exceptions to this trend are the specimens taken from the 3.2 mm gap (−3.2 mm overlap) build. Specimen B from this build shows no measurable performance that can be compared to the other tested specimens due to its nearly immediate failure. This specimen would typically be discarded but was included in order to accurately portray all results and findings. Specimen B shows how a specimen made with an intentional gap in the material deposition paths would be expected to perform. Specimen A (−3.2 mm overlap) performed very differently, even though it was taken from the same build. Specimen A had the highest ductility of the tested specimens by a notable margin. The results of the experimental tensile tests show that, in general, AFSD builds with a greater overlap width can expect greater and more consistent mechanical properties. As such, a build with a 0.0 mm overlap, or a small gap, will likely exhibit inferior tensile properties and inconsistent performance even within the same deposition.

For each fractured tensile specimen, SEM was used to perform post-mortem analysis of the fracture surfaces. Figure 13a shows the fracture surface of the specimen with 0.0 mm of overlap (A), which had the lowest quantified performance. This image shows the central portion of the fracture surface undergoing ductile fracture by showcasing the cup-and-ball, or dimpling, features commonly seen with micro-void coalescence seen in ductile failure, but this image also shows a very high angle of fracture with many sharp, flat regions indicative of poor ductility. Figure 13b shows the fracture surface of the specimen with 3.2 mm of overlap (A), which has a larger region of typical ductile features covering the left half of the image and sharp ridges on the right side containing some small pockets of shallow dimpling. Figure 13c,d show the surface of the specimen with 9.5 mm of overlap (A), which had the highest yield and ultimate strengths of the tested specimens. Figure 13c shows similar behavior as Figure 13b, with half of the fracture surface covered by dimpling, showcased at a higher magnification in Figure 13d, while the rest of the surface shows several layers of ridge-like features.

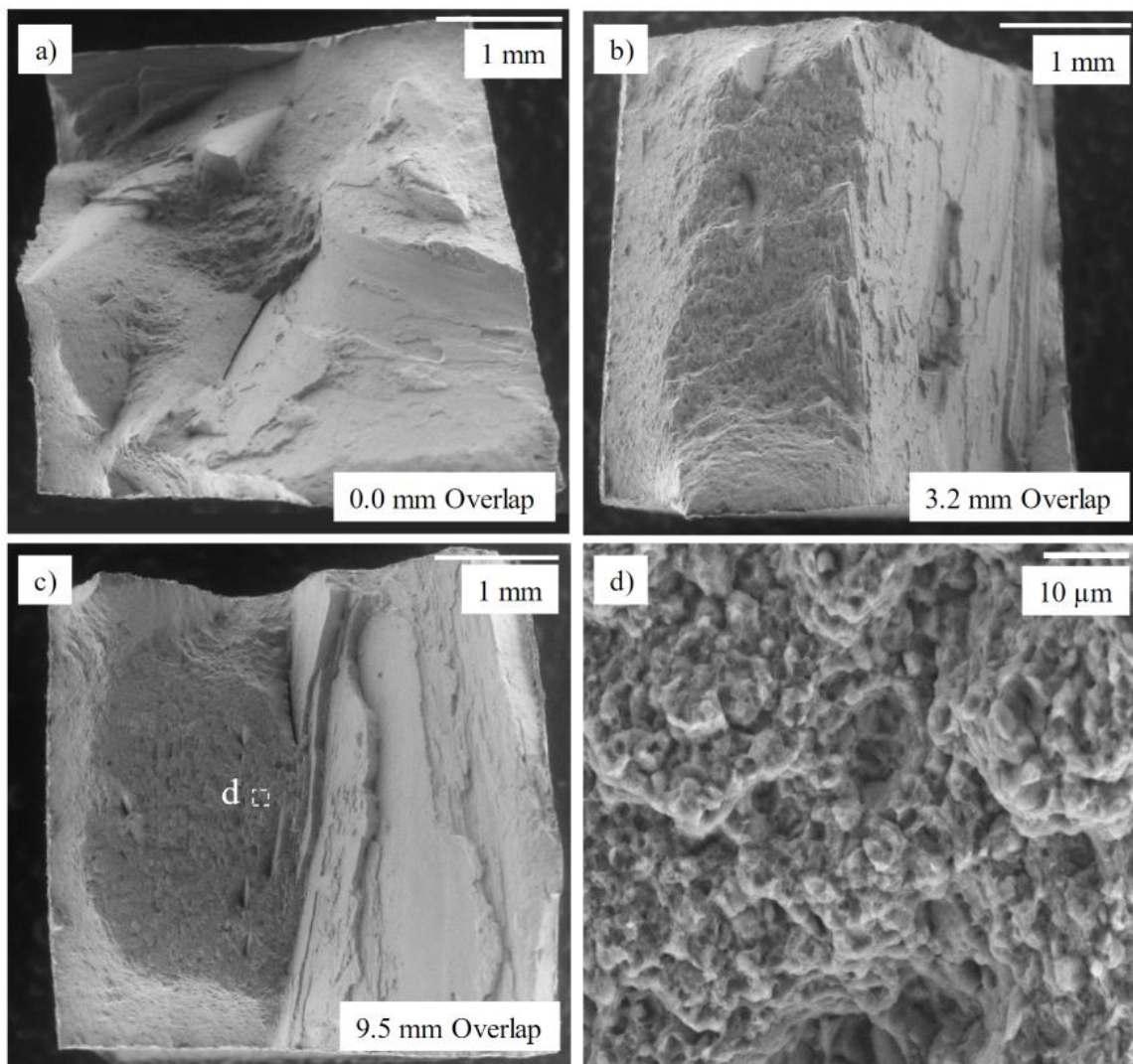


Figure 13. (a–c) SEM of tensile specimen fracture surfaces for non-negative overlap builds. (d) High magnification SEM image of dimpling effect from the specimen with 9.5 mm of overlap.

The observations made from the fracture surfaces confirm the results of the experimental tensile testing, with specimens undergoing a relatively low amount of ductility before complete failure compared to the feedstock specimen. The sharp angle of the resultant fracture surfaces compared to the direction of the applied force, especially in Figure 13a, suggests that the specimen experienced failure due to resultant shear stresses. The highest amount of ductility from the tested specimens only just exceeded half of that of the tested feedstock material, as shown in Table 4. These specimens are detailed and discussed separately in Figure 14.

Figure 14a,b show the fracture surface of the specimen with -3.2 mm of overlap (A), the specimen with the highest ductility from the overlap build specimens. Figure 14a shows a representative fracture surface primarily covered in dimpling, showcased in Figure 14b, which is expected given its relatively higher ductility. The ridge-like features previously observed are present in this fracture surface as well, primarily in the upper-left region of the image, but these ridges have small, dimpled regions across the surface. Figure 14c,d show the fracture surface of the specimen with -3.2 mm of overlap (B), which failed almost immediately upon mechanical loading. This fracture surface shows a wide range of features, with sharp, jagged cliffs across the bottom half of the surface, and a relatively smooth region across the top half, with very large cracks throughout the entire surface. It is worth noting a small region of ductility, magnified in Figure 14d, where dimpling occurs

in a small pocket amidst several jagged points and cracks was observed. This specimen failed rapidly with minimal ductility. The inconsistency between the specimens shown in Figure 14 further suggests that overlapping material is necessary to maintain the integrity of a large-scale build using AFSD.

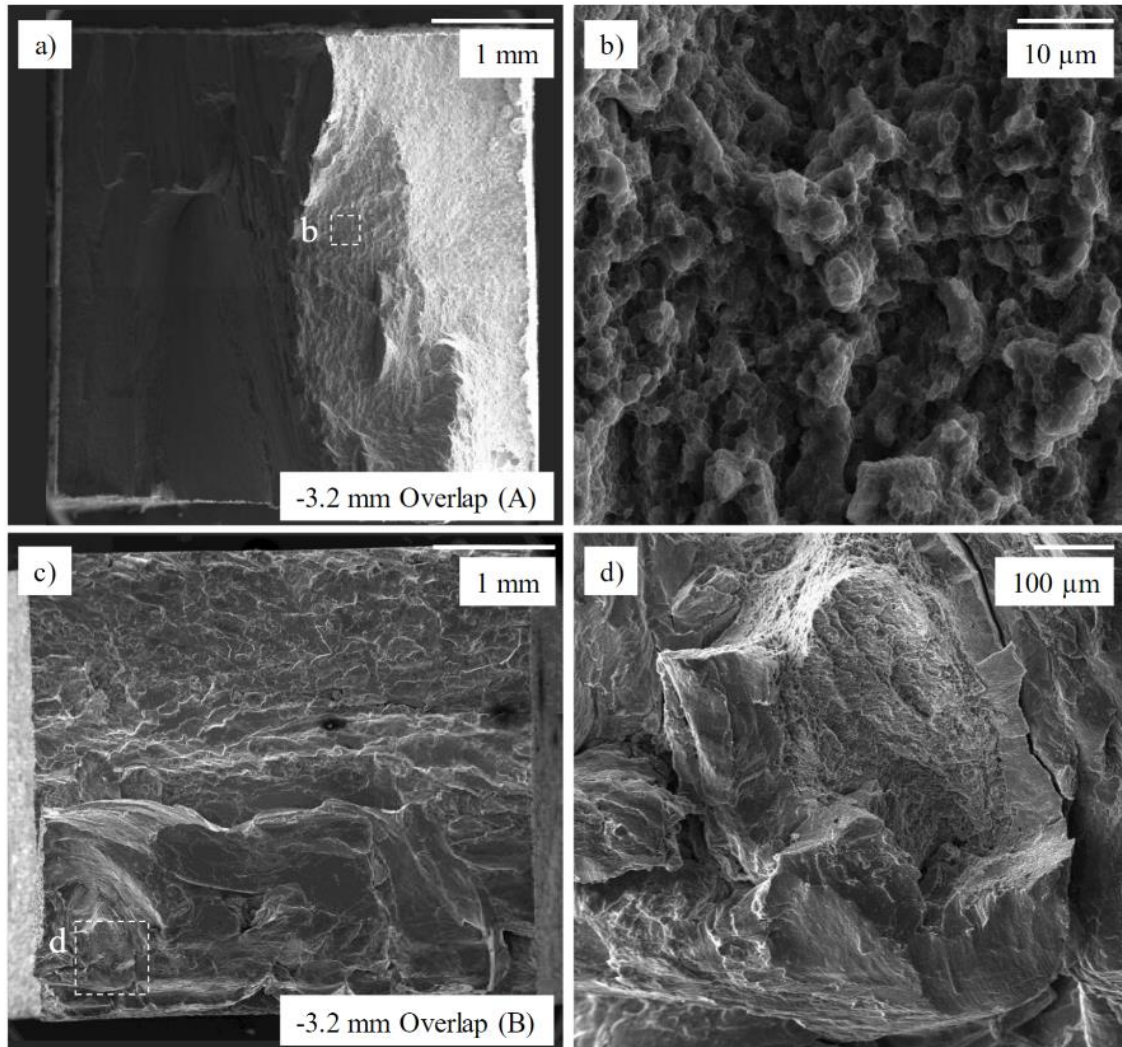


Figure 14. (a) SEM of tensile specimen fracture surfaces for the specimen with 3.2 mm of overlap (A). (b) High magnification image of dimpling effect observed in the specimen with -3.2 mm of overlap (A). (c) SEM of tensile specimen fracture surfaces for the specimen with -3.2 mm of overlap (B). (d) High magnification image of fracture surface geometry observed in the specimen with -3.2 mm of overlap (B).

4. Discussion

This present study evaluated the mechanical properties of as-deposited AA7075 with varying amounts of deposition path overlapping. Deposition hardness and grain size showed only small amounts of variation between samples with no apparent relationship to the overlap region width. The average grain size remained approximately 4 microns in the deposited overlapping region, which is similar to AFSD experiments reported elsewhere [39,44,45]. The average deposition hardness, ranging from 120 Hv to 135 Hv, is comparable to work focusing on the repair of AA7075 using AFSD performed by Stubblefield et al. (2022), where a hardness of 130 Hv was reported in the AFSD-repaired region [22], as well as work done by Avery et al. (2020) on the fatigue behavior of as-deposited AA7075, which reported a hardness of 125 Hv after natural aging [32]. The

hardness gradient observed throughout the TMAZ and HAZ of samples in this present study follows a similar trend documented by Robson et al. (2007) [46], where the hardness decreases significantly outside of the nugget zone due to the excess amount of heat put into the material during friction-stir processes.

The experimental tensile data shows a range of results that generally follows the trend in which increasing the overlap region width increases tensile strength within the overlap region when all other process parameters are held constant. While the tested specimens performed below the T6 feedstock material's strength and ductility, they did perform similarly to AA7075 material that has undergone FSW [38]. The tensile properties of the specimen with 9.5 mm of overlap (A), which achieved a UTS of 434 MPa compared to the feedstock material (583 MPa), illustrates that while as-deposited material will produce components with inferior mechanical properties when compared to the feedstock material, there was a clear benefit in overlapping the deposition paths to maintain the performance level of friction-stir processed material.

In order to produce large-scale components using AFSD in practical applications, a minimum amount of material should be overlapped between deposition passes in order to ensure that proper mixing and metallurgical bonding occurs and the desired benefits of the AFSD process are maintained throughout the build. As a near-net shape process, there will still be post-deposition machining and processing to produce a finished component, and the necessary amount of overlapping material will vary from build to build. With an increased overlap region comes improved mixing but less efficient use of material and longer deposition times. Excessive overlap will create diminished returns with respect to material strength while still greatly increasing the cost to produce components. For a relatively large, featureless deposition region, an overlap region width of 6.35–9.53 mm is recommended, assuming that the tool face has similar geometry to the one used in this study, and all other operating parameters are held constant. This overlapping value is equivalent to approximately 25% of the tool face and deposition width, which correlates to the track overlap ratio commonly used in directed energy deposition [47]. This value can be selectively increased as needed to work around potential features in order to reduce machining time, but a reduced overlap width would likely sacrifice the strength of the final component.

5. Conclusions

This study is the first to examine the effect of deposition pass overlap width on AFSD builds made from a high strength aluminum alloy. This work further assesses the viability of AFSD for a wide range of applications, proving that it can maintain as-deposited material properties over larger builds compared to single-track depositions. The following can be concluded:

1. AFSD builds with sufficient overlapping deposition paths will produce components with material properties that are comparable to single-row AFSD deposits of high-strength AA7075 in the as-deposited condition.
2. Less than 25% of the deposition width of the overlap may not be sufficient to achieve proper metallurgical bonding and material mixing between separate passes, and thus risks the formation of voids and cracks within the interface boundary.
3. Increasing the amount of overlapping material enhances ductility within the material. A small amount of overlap, or even a gap, will create inconsistent material properties due to non-uniform bonding.

For future work, supplemental experiments could be performed to evaluate the effect of overlapping deposition passes by focusing on knowledge gaps that were not addressed in this study. One point of interest would be quantifying the tensile behavior for specimens made with an overlap width larger than 38% of the deposition width, which is equal to 9.5 mm in this experiment. These specimens would have to be taken from a wider build made with multiple overlapping regions in order to accommodate the specimen size, while ensuring that the gage section of the tensile specimen is still composed of overlapping

material. An additional study could examine the vertical build direction properties of material within the overlap region by producing taller builds composed of several more layers of deposited material.

Author Contributions: Conceptualization, M.M.M., M.R.K., A.D.L., P.G.A. and J.B.J.; methodology, L.P.C. and M.B.W.; formal analysis, L.P.C., M.B.W., L.N.B., M.M.M., M.R.K., A.D.L., P.G.A. and J.B.J.; investigation, L.P.C. and M.B.W.; writing—original draft preparation, L.P.C.; writing—review and editing, L.N.B., M.R.K., P.G.A. and J.B.J. All authors have read and agreed to the published version of the manuscript.

Funding: This research was funded by US Army Combat Capabilities Development Command (DEVCOM) Ground Vehicle System Command (GVSC).

Institutional Review Board Statement: Not applicable.

Informed Consent Statement: Not applicable.

Data Availability Statement: Data is contained within the article. Additional data sharing is not available due to the private contract that provided funding for this research.

Acknowledgments: The authors would like to thank Harish Rao for his assistance in preparing the metallurgical samples. In addition, the authors would like to thank the US Army Combat Capabilities Development Command (DEVCOM) Ground Vehicle System Command (GVSC) for the financial support of this project. Finally, the authors would like to thank the Baylor University Point-of-Need Innovations (PONI) Center and the Center for Microscopy and Imaging for the use of resources and assistance.

Conflicts of Interest: The authors declare that they have no known competing financial interests or personal relationships that could have appeared to influence the work reported in this paper.

References

1. Reschetnik, W.; Brüggemann, J.-P.; Aydinöz, M.; Grydin, O.; Hoyer, K.-P.; Kullmer, G.; Richard, H. Fatigue crack growth behavior and mechanical properties of additively processed EN AW-7075 aluminium alloy. *Procedia Struct. Integr.* **2016**, *2*, 3040–3048. [[CrossRef](#)]
2. Montero-Sistiaga, M.L.; Mertens, R.; Vrancken, B.; Wang, X.; Van Hooreweder, B.; Kruth, J.-P.; Van Humbeeck, J. Changing the alloy composition of Al7075 for better processability by selective laser melting. *J. Mater. Process. Technol.* **2016**, *238*, 437–445. [[CrossRef](#)]
3. Fuller, C.B.; Mahoney, M.W.; Calabrese, M.; Micono, L. Evolution of microstructure and mechanical properties in naturally aged 7050 and 7075 Al friction stir welds. *Mater. Sci. Eng. A* **2010**, *527*, 2233–2240. [[CrossRef](#)]
4. Kamp, N.; Sullivan, A.; Tomasi, R.; Robson, J.D. Modelling of heterogeneous precipitate distribution evolution during friction stir welding process. *Acta Mater.* **2006**, *54*, 2003–2014. [[CrossRef](#)]
5. Joshi, S.S.; Patil, S.M.; Mazumder, S.; Sharma, S.; Riley, D.A.; Dowden, S.; Banerjee, R.; Dahotre, N.B. Additive friction stir deposition of AZ31B magnesium alloy. *J. Magnes. Alloys* **2022**, *10*, 2404–2420. [[CrossRef](#)]
6. Hassan, K.A.A.; Norman, A.F.; Price, D.A.; Prangnell, P.B. Stability of nugget zone grain structures in high strength Al-alloy friction stir welds during solution treatment. *Acta Mater.* **2003**, *51*, 1923–1936. [[CrossRef](#)]
7. Yu, H.Z.; Jones, M.E.; Brady, G.W.; Griffiths, R.J.; Garcia, D.; Rauch, H.A.; Cox, C.D.; Hardwick, N. Non-beam-based metal additive manufacturing enabled by additive friction stir deposition. *Scr. Mater.* **2018**, *153*, 122–130. [[CrossRef](#)]
8. Ghadimi, H.; Ding, H.; Emanet, S.; Talachian, M.; Cox, C.; Eller, M.; Guo, S. Hardness Distribution of Al2050 Parts Fabricated Using Additive Friction Stir Deposition. *Materials* **2023**, *16*, 1278. [[CrossRef](#)] [[PubMed](#)]
9. Su, J.-Q.; Nelson, T.W.; Mishra, R.; Mahoney, M. Microstructural investigation of friction stir welded 7050-T651 aluminium. *Acta Mater.* **2003**, *51*, 713–729. [[CrossRef](#)]
10. Sakai, T.; Belyakov, A.; Kaibyshev, R.; Miura, H.; Jonas, J.J. Dynamic and post-dynamic recrystallization under hot, cold and severe plastic deformation conditions. *Prog. Mater. Sci.* **2014**, *60*, 130–207. [[CrossRef](#)]
11. Kamp, N.; Sullivan, A.; Robson, J.D. Modelling of friction stir welding of 7xxx aluminium alloys. *Mater. Sci. Eng. A* **2007**, *466*, 246–255. [[CrossRef](#)]
12. Sullivan, A.; Robson, J.D. Microstructural properties of friction stir welded and post-weld heat-treated 7449 aluminium alloy thick plate. *Mater. Sci. Eng. A* **2008**, *478*, 351–360. [[CrossRef](#)]
13. Yoder, J.K.; Griffiths, R.J.; Yu, H.Z. Deformation-based additive manufacturing of 7075 aluminum with wrought-like mechanical properties. *Mater. Des.* **2021**, *198*, 109288. [[CrossRef](#)]

14. Griffiths, R.J.; Garcia, D.; Song, J.; Vasudevan, V.K.; Steiner, M.A.; Cai, W.; Yu, H.Z. Solid-state additive manufacturing of aluminum and copper using additive friction stir deposition: Process-microstructure linkages. *Materialia* **2021**, *15*, 100967. [[CrossRef](#)]
15. Joshi, S.S.; Sharma, S.; Radhakrishnan, M.; Pantawane, M.V.; Patil, S.M.; Jin, Y.; Yang, T.; Riley, D.A.; Banerjee, R.; Dahotre, N.B. A multi modal approach to microstructure evolution and mechanical response of additive friction stir deposited AZ31B Mg alloy. *Sci. Rep.* **2022**, *12*, 13234. [[CrossRef](#)] [[PubMed](#)]
16. Yoder, J.K.; Hahn, G.D.; Zhao, N.; Brennan, R.E.; Cho, K.; Yu, H.Z. Additive friction stir deposition-enabled upcycling of automotive cast aluminum chips. *Addit. Manuf. Lett.* **2023**, *4*, 100108. [[CrossRef](#)]
17. Garcia, D.; Hartley, W.D.; Rauch, H.A.; Griffiths, R.J.; Wang, R.; Kong, Z.J.; Zhu, Y.; Yu, H.Z. In situ investigation into temperature evolution and heat generation during additive friction stir deposition: A comparative study of Cu and Al-Mg-Si. *Addit. Manuf.* **2020**, *34*, 101386. [[CrossRef](#)]
18. Jin, Y.; Yang, T.; Wang, T.; Dowden, S.; Neogi, A.; Dahotre, N.B. Behavioral simulations and experimental evaluations of stress induced spatial nonuniformity of dynamic bulk modulus in additive friction stir deposited AA 6061. *J. Manuf. Process* **2023**, *94*, 454–465. [[CrossRef](#)]
19. Mason, C.; Rodriguez, R.; Avery, D.; Phillips, B.; Bernarding, B.; Williams, M.; Cobbs, S.; Jordon, J.; Allison, P. Process-structure-property relations for as-deposited solid-state additively manufactured high-strength aluminum alloy. *Addit. Manuf.* **2021**, *40*, 101879. [[CrossRef](#)]
20. Mishra, R.S.; Ma, Z.Y. Friction stir welding and processing. *Mater. Sci. Eng. R Rep.* **2005**, *50*, 1–78. [[CrossRef](#)]
21. Glenn, J.; Dean, L.; Wright, A.; Hovanski, Y. Closed-Loop PID Temperature Control of Additive Friction Stir Deposition. In *Friction Stir Welding and Processing XII*; Hovanski, Y., Sato, Y., Upadhyay, P., Naumov, A.A., Kumar, N., Eds.; Springer Nature: Cham, Switzerland, 2023; pp. 15–25. [[CrossRef](#)]
22. Stubblefield, G.G.; Williams, M.B.; Munther, M.; Tew, J.Z.; Rowe, R.A.; Barkey, M.E.; Jordon, J.B.; Allison, P.G. Ballistic Evaluation of Aluminum Alloy (AA) 7075 Plate Repaired by Additive Friction Stir Deposition Using AA7075 Feedstock. *J. Dyn. Behav. Mater.* **2023**, *9*, 79–89. [[CrossRef](#)]
23. Babaniaris, S.; Jiang, L.; Varma, R.K.; Farabi, E.; Dorin, T.; Barnett, M.; Fabijanic, D. Precipitation in AA6063 produced from swarf using additive friction stir deposition. *Addit. Manuf. Lett.* **2022**, *3*, 100096. [[CrossRef](#)]
24. Martin, L.P.; Luccitti, A.; Walluk, M. Repair of aluminum 6061 plate by additive friction stir deposition. *Int. J. Adv. Manuf. Technol* **2022**, *118*, 759–773. [[CrossRef](#)]
25. Martin, L.P.; Luccitti, A.; Walluk, M. Evaluation of Additive Friction Stir Deposition for the Repair of Cast Al-1.4Si-1.1Cu-1.5Mg-2.1Zn. *J. Manuf. Sci. Eng.* **2022**, *144*, 061006. [[CrossRef](#)]
26. Robinson, T.W.; Williams, M.B.; Rao, H.M.; Kinser, R.P.; Allison, P.G.; Jordon, J.B. Microstructural and Mechanical Properties of a Solid-State Additive Manufactured Magnesium Alloy. *J. Manuf. Sci. Eng.* **2022**, *144*, 061013. [[CrossRef](#)]
27. Al-Fadhalah, K.J.; Almazrouee, A.I.; Aloraier, A.S. Microstructure and mechanical properties of multi-pass friction stir processed aluminum alloy 6063. *Mater. Des* **2014**, *53*, 550–560. [[CrossRef](#)]
28. Ma, Z.Y.; Sharma, S.R.; Mishra, R.S. Effect of multiple-pass friction stir processing on microstructure and tensile properties of a cast aluminum–silicon alloy. *Scr. Mater.* **2006**, *54*, 1623–1626. [[CrossRef](#)]
29. Phillips, B.; Mason, C.; Beck, S.; Avery, D.; Doherty, K.; Allison, P.; Jordon, J. Effect of parallel deposition path and interface material flow on resulting microstructure and tensile behavior of Al-Mg-Si alloy fabricated by additive friction stir deposition. *J. Mater. Process. Technol.* **2021**, *295*, 117169. [[CrossRef](#)]
30. Kumar, P.V.; Reddy, G.M.; Rao, K.S. Microstructure, mechanical and corrosion behavior of high strength AA7075 aluminium alloy friction stir welds—Effect of post weld heat treatment. *Def. Technol.* **2015**, *11*, 362–369. [[CrossRef](#)]
31. Leng, J.; Ren, B.; Dong, Y.; Wu, H. Grain Refinement and Strengthening Mechanism Analysis of an Ultrahigh Strength Sc(Er)–Zr–7075 Aluminum Alloy. *Phys. Met. Metallogr.* **2021**, *122*, 1597–1604. [[CrossRef](#)]
32. Avery, D.Z.; Phillips, B.J.; Mason, C.J.T.; Palermo, M.; Williams, M.B.; Cleek, C.; Rodriguez, O.L.; Allison, P.G.; Jordon, J.B. Influence of Grain Refinement and Microstructure on Fatigue Behavior for Solid-State Additively Manufactured Al-Zn-Mg-Cu Alloy. *Metall. Mater. Trans. A* **2020**, *51*, 2778–2795. [[CrossRef](#)]
33. Park, J.K.; Ardell, A.J. Microstructures of the commercial 7075 Al alloy in the T651 and T7 tempers. *Metall. Trans. A* **1983**, *14*, 1957–1965. [[CrossRef](#)]
34. Elatharasan, G.; Kumar, V.S.S. Corrosion Analysis of Friction Stir-welded AA 7075 Aluminium Alloy. *Stroj. Vestn. -J. Mech. Eng* **2014**, *60*, 29–34. [[CrossRef](#)]
35. Veeravalli, R.R.; Nallu, R.; Sarcar, M.M.M. Mechanical and tribological properties of AA7075–TiC metal matrix composites under heat treated (T6) and cast conditions. *J. Mater. Res. Technol.* **2016**, *5*, 377–383. [[CrossRef](#)]
36. Griffiths, R.J.; Petersen, D.T.; Garcia, D.; Yu, H.Z. Additive Friction Stir-Enabled Solid-State Additive Manufacturing for the Repair of 7075 Aluminum Alloy. *Appl. Sci.* **2019**, *9*, 3486. [[CrossRef](#)]
37. Duong, H.D.; Okazaki, M.; Tran, T.H. Influence of probe length on the formation of an interface in friction stir welded T-lap joints. *Mater. Manuf. Process* **2021**, *36*, 693–701. [[CrossRef](#)]
38. Shahabuddin; Dwivedi, V.K.; Sharma, A. Influence on the Tensile Properties of AA7075-T6 under Different Conditions during friction stir welding process. *IOP Conf. Ser. Mater. Sci. Eng.* **2019**, *691*, 012001. [[CrossRef](#)]

39. Avery, D.Z.; Cleek, C.; Phillips, B.J.; Rekha, M.Y.; Kinser, R.P.; Rao, H.; Brewer, L.N.; Allison, P.G.; Jordon, J.B. Evaluation of Microstructure and Mechanical Properties of Al-Zn-Mg-Cu Alloy Repaired via Additive Friction Stir Deposition. *J. Eng. Mater. Technol.* **2022**, *144*, 031003. [[CrossRef](#)]
40. E08 Committee; Test Method for Strain-Controlled Fatigue Testing. ASTM International: West Conshohocken, PA, USA, 2021. [[CrossRef](#)]
41. E04 Committee; Test Method for Microindentation Hardness of Materials. ASTM International: West Conshohocken, PA, USA, 2022. [[CrossRef](#)]
42. E04 Committee; Test Methods for Determining Average Grain Size. ASTM International: West Conshohocken, PA, USA, 2021. [[CrossRef](#)]
43. Jordon, J.B.; Horstemeyer, M.F.; Solanki, K.; Bernard, J.D.; Berry, J.T.; Williams, T.N. Damage characterization and modeling of a 7075-T651 aluminum plate. *Mater. Sci. Eng. A* **2009**, *527*, 169–178. [[CrossRef](#)]
44. Yu, H.Z.; Mishra, R.S. Additive friction stir deposition: A deformation processing route to metal additive manufacturing. *Mater. Res. Lett.* **2021**, *9*, 71–83. [[CrossRef](#)]
45. Mishra, R.S.; Haridas, R.S.; Agrawal, P. Friction stir-based additive manufacturing. *Sci. Technol. Weld. Join* **2022**, *27*, 141–165. [[CrossRef](#)]
46. Robson, J.D.; Kamp, N.; Sullivan, A. Microstructural Modelling for Friction Stir Welding of Aluminium Alloys. *Mater. Manuf. Process* **2007**, *22*, 450–456. [[CrossRef](#)]
47. Ahn, D.-G. Directed Energy Deposition (DED) Process: State of the Art. *Int. J. Precis. Eng. Manuf.-Green. Technol.* **2021**, *8*, 703–742. [[CrossRef](#)]

Disclaimer/Publisher’s Note: The statements, opinions and data contained in all publications are solely those of the individual author(s) and contributor(s) and not of MDPI and/or the editor(s). MDPI and/or the editor(s) disclaim responsibility for any injury to people or property resulting from any ideas, methods, instructions or products referred to in the content.